colloids and interfaces

MDPI

Article

PVA-Stabilized Biogenic Selenium Nanoparticles: Physicochemical Properties and Ultrastructural Responses in Human Dermal Fibroblasts

José Armando Hernández-Díaz [1,†], Brian Ibe Da Silva-Trejo [2,3,4,†], Moisés Martínez-Velázquez [1], Soledad García-Morales [5], Edwin Bladimir Bonilla-Ascencio [6,7], Sergio Manuel Nuño-Donlucas [7], Rosario Ortiz-Hernández [8], Alberto Gutiérrez-Becerra [9], Zaira Yunuen García-Carvajal [1,*] and Cristina Velasquillo [2,3,4,*]

1 Medical and Pharmaceutical Biotechnology, Center for Research and Assistance in Technology and Design of the State of Jalisco A.C., Guadalajara 44270, Jalisco, Mexico; johernandez_al@ciatej.edu.mx (J.A.H.-D.); mmartinez@ciatej.mx (M.M.-V.)
2 Monterrey Institute of Technology and Higher Education, Mexico City Campus, Tlalpan 14380, Ciudad de México, Mexico; a01663903@exatec.tec.mx
3 Tissue Engineering, Cell Therapy and Regenerative Medicine Unit, Luis Guillermo Ibarra Ibarra National Rehabilitation Institute, Tlalpan, Mexico City 14389, Mexico
4 Department of Mechatronics, School of Engineering and Sciences, Monterrey Institute of Technology and Higher Education, Mexico City Campus, Mexico City 14380, Mexico
5 Plant Biotechnology, Secretariat of Science, Humanities, Technology and Innovation—Center for Research and Assistance in Technology and Design of the State of Jalisco A.C., Zapopan 45019, Jalisco, Mexico; smorales@ciatej.mx
6 School of Chemistry, Faculty of Natural Sciences and Mathematics, University of El Salvador, San Salvador 1101, El Salvador; edwin.bonilla@ues.edu.sv
7 Department of Chemical Engineering, University Center for Exact Sciences and Engineering, University of Guadalajara, Guadalajara 44430, Jalisco, Mexico; sergio.nuno@academicos.udg.mx
8 G. Hebert Vázquez Nin, Electron Microscopy Laboratory, Faculty of Sciences, National Autonomous University of Mexico, Coyoacán 04510, Ciudad de México, Mexico; r_oh@ciencias.unam.mx
9 Department of Basic and Applied Sciences, Tonalá University Center (CUTonalá), University of Guadalajara, Tonala 45425, Jalisco, Mexico; alberto.gbecerra@academicos.udg.mx
* Correspondence: zgarcia@ciatej.mx (Z.Y.G.-C.); cristina.velas@tec.mx or mvelasquillo@ciencias.unam.mx (C.V.)
† These authors contributed equally to this work.

Abstract

Biogenic selenium nanoparticles (SeNPs) offer promising biomedical properties, although the polymeric environment can influence their physicochemical stability and cellular interactions. In this study, SeNPs synthesized using *Amphipterygium glaucum* leaf extract were incorporated into a medium-molecular-weight poly(vinyl alcohol) (PVA) matrix to obtain a redispersible SeNPs@PVA89 nanocomposite. Spectroscopic, structural, morphological, thermal, and dispersion analyses showed that incorporating SeNPs preserved characteristic nanoscale and optical features while altering polymer organization. The hydrodynamic diameter increased from 153 to 320 nm, and the ζ-potential shifted from −53 to −22 mV, consistent with changes in the nanoparticle interfacial environment and a hydrated PVA layer. In human dermal fibroblasts, SeNPs@PVA89 induced concentration-dependent effects: metabolic activity was preserved at 3 and 6 μg/mL, whereas ≥12 μg/mL markedly reduced cell viability; at 3 μg/mL, morphology, F-actin organization, and wound closure were preserved. Nevertheless, confocal microscopy revealed punctate intracellular fluorescence, while transmission electron microscopy showed electron-dense material within membrane-bound vesicles, alongside mitochondrial fragmentation, cristae alterations, and rough endoplasmic reticulum remodeling. Although the elemental identity of these electron-dense structures was not directly confirmed, the findings are consistent with cellular interaction and vesicular sequestration of the nanosystem. Overall, PVA-stabilized biogenic SeNPs

Check for updates

Academic Editor: Ying Kuang

Received: 23 September 2026
Revised: 20 October 2026
Accepted: 23 October 2026
Published: 29 October 2026

Copyright: © 2026 by the authors. Licensee MDPI, Basel, Switzerland. This article is an open access article distributed under the terms and conditions of the Creative Commons Attribution (CC BY) license.

showed concentration-dependent cellular effects, with ultrastructural remodeling despite unchanged conventional cytocompatibility outcomes.

Keywords: selenium nanoparticles; poly(vinyl alcohol); biocompatibility; human dermal fibroblast; ultrastructural analysis

1. Introduction

Selenium nanoparticles (SeNPs) have attracted considerable interest for biomedical applications because their nanoscale dimensions and surface reactivity enable interactions with biological systems while offering antioxidant, antimicrobial, anti-inflammatory, and anticancer activities [1–4]. Compared with conventional inorganic and organic selenium compounds, SeNPs may provide a broader therapeutic window and reduced toxicity under appropriate exposure conditions [1,2]. However, their biological performance depends strongly on particle size, surface chemistry, aggregation state, and the stabilizing environment, making control of their physicochemical properties essential for reproducible biological applications.

Biogenic synthesis is an attractive strategy for producing SeNPs because plant-derived metabolites can act as both reducing and surface-capping agents. Polyphenols, flavonoids, terpenoids, proteins, and polysaccharides in plant extracts may participate in nanoparticle formation and remain adsorbed on the nanoparticle surface, influencing dispersion, surface charge, and biological interactions [5–8]. *Amphipterygium glaucum*, a medicinal plant native to Mexico, contains bioactive compounds capable of supporting the biosynthesis of SeNPs [5,6]. Nevertheless, biogenic nanoparticles remain susceptible to aggregation, oxidation, and changes in dispersion during processing, storage, and exposure to biological environments. These changes can alter nanoparticle availability and consequently modify cellular responses.

Polymeric stabilization offers a strategy to control nanoparticle dispersion and surface behavior. Poly(vinyl alcohol) (PVA) is a hydrophilic, biocompatible polymer widely used in biomedical nanocomposites because of its chemical versatility, high density of hydroxyl groups, and ability to interact with nanoparticle surfaces [9]. PVA association with nanoparticles can modify the local interfacial environment through hydrogen bonding and steric interactions, affecting hydrodynamic size, surface charge, aggregation behavior, and polymer-chain organization. Consequently, evaluating PVA-stabilized SeNPs requires characterizing not only nanoparticle morphology and composition, but also the physicochemical changes resulting from nanoparticle–polymer interactions.

Conventional viability measurements alone cannot fully establish the biological consequences of these physicochemical characteristics. Assays based on metabolic activity, cell morphology, cytoskeletal organization, and migration provide valuable information on overall cellular function, but they may not detect early subcellular responses to nanoparticle exposure [10–13]. Nanoparticles may interact with the plasma membrane, associate with intracellular vesicular compartments, and alter mitochondria or the endomembrane system before measurable loss of cellular viability occurs. Transmission electron microscopy (TEM) is therefore particularly valuable because it enables direct visualization of cellular ultrastructure and can reveal mitochondrial alterations, rough endoplasmic reticulum remodeling, and electron-dense intracellular structures at nanometer-scale resolution [13,14].

Despite growing interest in selenium-based nanomaterials, the relationship between polymer-mediated stabilization, physicochemical behavior, and early ultrastructural responses in normal human fibroblasts remains poorly characterized. In particular, functional cytocompatibility may not indicate the absence of subcellular alterations after exposure to

stabilized SeNP formulations. Therefore, this study aimed to characterize biogenic SeNPs synthesized using *A. glaucum* extract and stabilized in a medium-molecular-weight PVA matrix, and to investigate their interactions with human dermal fibroblasts. We integrated spectroscopic, morphological, structural, thermal, and dispersion analyses with metabolic activity, wound-closure, cytoskeletal, fluorescence, and ultrastructural evaluations. The novelty of this work lies in going beyond developing a redispersible PVA-stabilized SeNPs formulation: by combining physicochemical characterization with functional and ultrastructural analyses, we show that a nanocomposite may appear cytocompatible in conventional assays yet still induce ultrastructural alterations detectable by TEM. In addition, the nanocomposite's intrinsic fluorescence allowed us to examine its intracellular association by confocal microscopy, complementing the TEM observations.

2. Materials and Methods

2.1. Biogenic Selenium Nanoparticles

Biogenic selenium nanoparticles (SeNPs) were synthesized by reduction in sodium selenite (Na_2SeO_3) using *A. glaucum* leaf extract as the reducing and capping agent, following the procedure previously reported by Hernández-Díaz et al. [15]. The SeNPs used in the present study followed the same formulation previously reported by our group; however, whereas that earlier work employed an aerogel-based formulation evaluated primarily through conventional cytotoxicity assays, the SeNPs here were independently re-characterized by UV–Vis spectroscopy, FTIR, TEM, dynamic light scattering (DLS), and ζ-potential analysis and incorporated into a redispersible lyophilized PVA nanocomposite [16]. This approach allowed us to specifically characterize the SeNP–PVA interfacial environment and its relationship to ultrastructural, rather than purely viability-based, cellular responses.

2.2. Preparation of SeNPs@PVA89

A medium-molecular-weight poly(vinyl alcohol) (PVA; 89 kDa; Sigma-Aldrich, St. Louis, MO, USA) was used to prepare the SeNPs@PVA89 nanocomposite. A 4% (*w/v*) PVA aqueous solution was prepared in double-distilled water at 90 °C under continuous stirring at 700 rpm for 1 h. The solution was cooled to room temperature for 30 min and then exposed to ultraviolet irradiation for 20 min. Biogenic SeNPs (10 mg/mL) were dispersed in 100 µL of double-distilled water and sonicated at 45 °C for 15 min. The PVA solution was then added under aseptic conditions and vortexed until the dispersion became macroscopically homogeneous. The resulting formulation was allowed to equilibrate for 30 min, then frozen at −80 °C, and lyophilized using a LyoQuest freeze dryer (Telstar, Barcelona, Spain). The resulting SeNPs@PVA89 nanocomposite was stored under sterile conditions until further characterization and biological evaluation.

2.3. Physicochemical Characterization

2.3.1. UV–Vis Spectroscopy

UV–visible spectra of biogenic SeNPs, PVA89, and SeNPs@PVA89 were recorded over 200–500 nm using a NanoDrop 2000 spectrophotometer (Thermo Scientific, Waltham, MA, USA). Measurements were used to evaluate the characteristic absorption profile of the SeNPs before and after incorporation into the PVA matrix. Spectral data were processed using OriginPro 2024 (OriginLab Corporation, Northampton, MA, USA).

2.3.2. Fourier-Transform Infrared Spectroscopy

The chemical groups associated with biogenic SeNPs, PVA89, and SeNPs@PVA89 were analyzed by attenuated total reflectance Fourier-transform infrared spectroscopy (ATR-

FTIR) using a TENSOR II spectrometer (Bruker Optics, Billerica, MA, USA). Spectra were collected over 4000–400 cm^{-1}.

2.3.3. Transmission Electron Microscopy of Biogenic SeNPs

The morphology and primary particle size of biogenic SeNPs were evaluated by transmission electron microscopy (TEM) using a JEM-2100 microscope (JEOL, Tokyo, Japan) operated at 200 kV and equipped with a Gatan OneView 4K camera (Gatan, Inc., Pleasanton, CA, USA). Particle size was determined from representative TEM micrographs by measuring 102 individual nanoparticles. The particle-size distribution was shown as a histogram with a superimposed Gaussian curve for visualization in OriginPro 2024 (OriginLab Corporation, Northampton, MA, USA).

2.3.4. Dynamic Light Scattering (DLS) and Zeta Potential

The hydrodynamic diameter of SeNPs was determined by dynamic light scattering (DLS) using a Litesizer 500 instrument (Anton Paar, Graz, Austria). Aqueous dispersions (1 mL) with low turbidity were analyzed in a capillary cell at 25 °C. Measurements were acquired over 3 min using 60 runs, with five independent replicates per sample.

The zeta potential was determined using the same instrument and capillary cell with an acquisition time of 10 min, an applied voltage of 50 V, 1000 measurements, and three independent replicates per sample.

2.3.5. Scanning Electron Microscopy (SEM) and EDS

The morphology of SeNPs@PVA89 was examined by high-resolution scanning electron microscopy (SEM) using a JSM-IT300 microscope (JEOL, Tokyo, Japan). Samples were mounted on carbon adhesive tape, sputter-coated with gold, and observed at an accelerating voltage of 15–20 kV with magnifications ranging from 100× to 50,000×.

2.3.6. X-Ray Diffraction (XRD)

The crystalline structure of biogenic SeNPs, PVA89, and SeNPs@PVA89 was analyzed using an Empyrean X-ray diffractometer (Malvern Panalytical, Malvern, UK) with Cu Kα radiation (λ = 1.5406 Å). Samples were analyzed in reflection geometry on a flat-sample stage. Diffraction patterns were recorded in continuous scan mode over a 2θ range of 10–90°, using an operating voltage of 40 kV, a current of 35 mA, a step size of 0.0263°, and a scanning rate of 0.2188° s^{-1}. Phase identification of the biogenic SeNPs was performed using Match! v4.2 (Crystal Impact, Bonn, Germany) with the Crystallography Open Database (COD), and the unit cell parameters were determined from the indexed reflections. For PVA89, peak positions (2θ) were determined using Plot2 Pro v.2.8.0 (Mike Wesemann, Berlin, Germany), and interplanar spacings (d) were calculated using Bragg's law (λ = 2d sinθ, with λ = 1.5406 Å). The unit cell parameters of the monoclinic PVA crystal were then calculated from the (101), (200), and (111) reflections using Equation (1):

$$\frac{1}{d^2} = \frac{1}{sin^2(\beta)}\left(\frac{h^2}{a^2} + \frac{k^2\, sin^2(\beta)}{b^2} + \frac{l^2}{c^2} - \frac{2hl\, cos(\beta)}{a\, c}\right) \quad (1)$$

where h, k, and l are the Miller indices. The angles were fixed at $\alpha = \gamma = 90°$ and $\beta = 91.7°$, according to the monoclinic cell reported by Nitta et al. [17].

2.3.7. Differential Scanning Calorimetry (DSC)

The thermal behavior of PVA and SeNPs@PVA89 was evaluated by differential scanning calorimetry (DSC) using a Q2000 calorimeter (TA Instruments, New Castle, DE, USA). Samples were placed in aluminium sample pans and analyzed over a temperature range

of −70 to 250 °C at a heating rate of 10 °C min^{-1}. Two consecutive heating scans were performed for each sample to evaluate their thermal transitions.

2.4. Biological Evaluation

2.4.1. Cell Culture

Human adult dermal fibroblasts (HDFa; ATCC® PCS-201-012, American Type Culture Collection, Manassas, VA, USA) were cultured in MEM/F-12 medium (Gibco, Thermo Fisher Scientific, Waltham, MA, USA) supplemented with 10% fetal bovine serum (FBS; Corning Incorporated, Corning, NY, USA) and 1% antibiotic–antimycotic solution (Gibco, Thermo Fisher Scientific, Waltham, MA, USA). Cells were maintained at 37 °C in a humidified atmosphere containing 5% CO_2 and subcultured at approximately 80% confluence. All biological experiments were performed using passage-7 fibroblasts unless otherwise indicated.

2.4.2. MTT Metabolic Activity Assay

Human dermal fibroblasts were seeded in 96-well plates (Corning, Corning, NY, USA) at a density of 1×10^4 cells/well and allowed to attach for 24 h. We dispersed SeNPs@PVA89 in complete culture medium at 10 mg/mL and serially diluted to final concentrations of 3, 6, 12, 25, 50, 100, and 200 µg/mL. Cells were exposed to the corresponding formulation for 24 h. Following exposure, the medium containing SeNPs@PVA89 was removed, and MTT solution (Thiazolyl Blue Tetrazolium Bromide; Sigma-Aldrich, St. Louis, MO, USA) was added at a 1:10 (*v*/*v*) ratio. After incubation for 2.5 h at 37 °C, the MTT solution was removed, and the resulting formazan crystals were dissolved in a 1:1 (v/v) mixture of isopropanol (Sigma-Aldrich, St. Louis, MO, USA) and dimethyl sulfoxide (DMSO; Sigma-Aldrich, St. Louis, MO, USA). Absorbance was measured at 570 nm using an xMark™ Microplate Spectrophotometer (Bio-Rad Laboratories, Hercules, CA, USA). Metabolic activity was expressed relative to untreated cells, which were considered 100%. Cell viability was calculated using the following Equation (2):

$$Cell\ Viability\ (\%) = \frac{Abs_{(sample)}}{Abs_{(control)}} \times 100 \quad (2)$$

where Abs(sample) is the absorbance of cells treated with the corresponding formulation, and Abs(control) is the absorbance of untreated control cells, which was considered to represent 100% cell viability.

2.4.3. In Vitro Wound Healing (Scratch) Assay

Human dermal fibroblasts were seeded in 24-well plates at a density of 2×10^4 cells/well and cultured for 24 h. A linear scratch was subsequently generated across the cell monolayer using a sterile pipette tip, after which cells were exposed to SeNPs@PVA89 at 3, 25, 100, or 200 µg/mL. Images were acquired immediately after scratching (T0) and after 24 and 48 h using an Axio Observer A1 inverted microscope (Carl Zeiss, Oberkochen, Germany). At the end of the experiment, cells were stained with crystal violet (Sigma-Aldrich, St. Louis, MO, USA) to facilitate visualization of the monolayer. The remaining cell-free area was quantified using ImageJ software version 1.54r (National Institutes of Health, Bethesda, MD, USA), and wound closure was calculated relative to the initial scratch area.

2.5. Cellular Imaging

2.5.1. Intrinsic Fluorescence of SeNPs@PVA89

Human dermal fibroblasts were seeded on glass coverslips (Corning, Corning, NY, USA) in 24-well plates at a density of 2×10^4 cells/coverslip and allowed to attach for 24 h. Cells were then exposed to 3 µg/mL SeNPs@PVA89 for 24 h. Following exposure,

cells were fixed with 1% paraformaldehyde (PFA; Sigma-Aldrich, St. Louis, MO, USA)and examined by confocal laser scanning microscopy using an LSM 880 microscope (Carl Zeiss, Oberkochen, Germany).

2.5.2. Fluorescence Staining of F-Actin and Cell Nuclei

Human dermal fibroblasts were seeded on glass coverslips Corning, Corning, NY, USA) in 24-well plates at a density of 2×10^4 cells/coverslip and exposed to 3 µg/mL SeNPs@PVA89 for 24 h. Cells were subsequently fixed with 4% PFA (Sigma-Aldrich, St. Louis, MO, USA), permeabilized with 0.01% Tween-20 (Bio-Rad Laboratories, Hercules, CA, USA) in PBS (Gibco, Thermo Fisher Scientific, Waltham, MA, USA), and stained with phalloidin–fluorescein conjugate (Santa Cruz Biotechnology, Dallas, TX, USA) diluted (1:1000 in PBS containing 1% bovine serum albumin (BSA; Thermo Fisher Scientific, Waltham, MA, USA)) to visualize F-actin. Cell nuclei were counterstained with 0.0002% DAPI (Abcam, Cambridge, UK). Samples were examined using epifluorescence and confocal microscopy.

2.5.3. Transmission Electron Microscopy (TEM) of Fibroblasts

Human dermal fibroblasts (HDF) were divided into untreated control and SeNPs@PVA89-exposed groups. Treated cells were exposed to 3 µg/mL SeNPs@PVA89 for 24 h under standard culture conditions (37 °C, 5% CO_2). We selected this concentration based on MTT and wound-closure assays, which showed preserved metabolic activity and normal wound-closure behavior. After exposure, approximately 3×10^6 cells per condition were harvested and fixed in 100 mM cacodylate buffer (Sigma-Aldrich, St. Louis, MO, USA), pH 7.2, containing 2.5% glutaraldehyde (Electron Microscopy Sciences, Hatfield, PA, USA) and 4% PFA (Electron Microscopy Sciences, Hatfield, PA, USA) for 2 h at room temperature (20–25 °C). Cells were pelleted by centrifugation at 608× *g* for 5 min, washed four times with cacodylate buffer, and centrifuged after each wash. Samples were post-fixed with 1% osmium tetroxide (Electron Microscopy Sciences, Hatfield, PA, USA) for 1 h at room temperature, washed six times with cacodylate buffer, dehydrated through a graded ethanol series, and subsequently incubated in acetone for 5 min. Cell pellets were embedded in Durcupan ACM resin (Sigma-Aldrich, St. Louis, MO, USA; Cat. No. 44610) and polymerized at 60 °C for 48 h. Ultrathin sections of approximately 60 nm were collected on Formvar-coated copper grids, stained with 4% uranyl acetate for 20 min, followed by 0.35% lead citrate for 10 min (both from Electron Microscopy Sciences, Hatfield, PA, USA), and examined using a JEOL JEM-1010 transmission electron microscope (JEOL, Tokyo, Japan) operated at 100 kV. Untreated HDF processed under the same conditions were used as the ultrastructural control.

2.6. Statistical Analysis

Data are presented as mean ± standard deviation (SD) from three independent biological replicates. MTT data were analyzed using repeated-measures one-way ANOVA with the Geisser–Greenhouse correction followed by Tukey's multiple-comparisons test. Wound-closure data were analyzed by two-way ANOVA followed by Tukey's multiple-comparisons test. Statistical significance was established at $p < 0.05$. Analyses were performed using GraphPad Prism version 9 (GraphPad Software, San Diego, CA, USA).

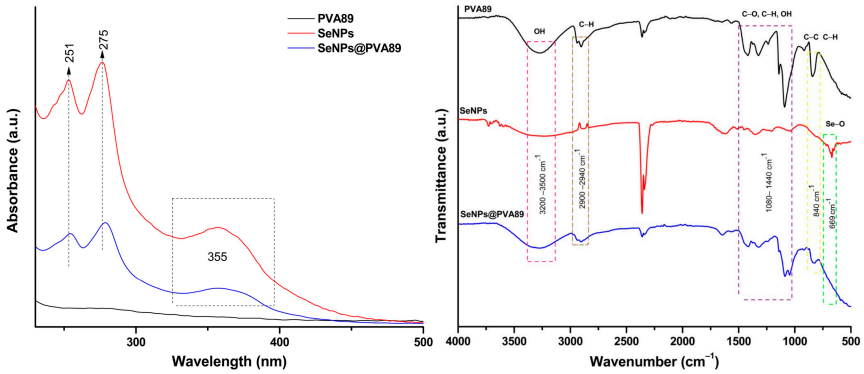
3. Results and Discussion

3.1. UV–Vis and FTIR Spectroscopy

The biogenic SeNPs used in this study match the formulation previously synthesised and reported by Hernández-Díaz et al. [15]. Before incorporating them into the PVA matrix,

we independently recharacterized the nanoparticles under the experimental conditions used in the present study.

As shown in Figure 1A, free SeNPs showed an absorption band centered at approximately 275 nm. This band was maintained after incorporation into the PVA matrix, with no appreciable shift in the absorption maximum. Absorbance intensity decreased for SeNPs@PVA89. This difference may be related to changes in the effective nanoparticle concentration, light scattering, or the local environment of the particles within the polymer matrix [18,19]. Interactions between PVA hydroxyl groups and surface-associated molecules on the biogenic SeNPs may also contribute to this change [20]. However, since the absorption maximum remained at approximately the same wavelength, no substantial change in the characteristic optical response of the SeNPs was observed after incorporation into PVA. The UV–Vis profile was also maintained after freeze-drying and reconstitution, indicating that the processing procedure did not produce an evident change in the optical characteristics of the nanoparticles [21].



(**A**) (**B**)

Figure 1. UV–Vis and FTIR spectroscopic characterization of free SeNPs and SeNPs@PVA89. (**A**) UV–Vis absorption spectra of free SeNPs and SeNPs@PVA89 after incorporation into the PVA matrix. (**B**) FTIR spectra showing the characteristic absorption bands of free SeNPs and SeNPs@PVA89 following NC formation.

The FTIR spectra are shown in Figure 1B. Free SeNPs exhibited bands associated with functional groups derived from phytochemical constituents of the *A. glaucum* extract, which have been previously associated with the reduction and stabilization of the biogenic nanoparticles [15]. Bands assigned to Se–O vibrations were also observed, consistent with the presence of surface-associated selenium species [5].

After incorporation into PVA, the SeNPs@PVA89 spectrum showed the polymer's characteristic bands, along with changes in several regions of the spectrum. The broad O–H stretching band shifted from approximately 3283 to 3300 cm^{-1} and became broader. This change is consistent with a modified hydrogen-bonding environment of the PVA hydroxyl groups after nanoparticle incorporation. The CH_2 stretching and deformation bands were also observed near 2940 and 1417 cm^{-1}, respectively [22,23].

In the fingerprint region, the band near 1140 cm^{-1} decreased in intensity after nanocomposite formation. This band is commonly associated with C–O stretching and has been used as an indicator of PVA crystalline organization [24]. The observed change may therefore reflect changes in polymer-chain organization. The band near 1090 cm^{-1} also changed after incorporating SeNPs, splitting into two bands. This behavior suggests a change in the local vibrational environment of the C–O groups [25].

The band near 843 cm^{-1} decreased in intensity and shifted to approximately 833 cm^{-1}. This region has been associated with C–C skeletal and out-of-plane C–H vibrations in

PVA [22,26]. The observed shift may reflect changes in the local conformation or organization of the polymer chains after nanoparticles incorporation. In addition, the band near 669 cm^{-1} observed in the free SeNPs was attenuated and partially overlapped in the SeNPs@PVA89 spectrum. This change may be associated with modification of the vibrational environment of surface-associated selenium species within the polymer matrix [27].

Overall, the UV–Vis results show that the characteristic absorption of the biogenic SeNPs was maintained after incorporation into PVA, freeze-drying, and reconstitution. The FTIR spectra showed changes in the O–H stretching region and, in several bands, associated with the PVA backbone, together with attenuation of the band associated with surface selenium species. These changes are consistent with interactions between the biogenic SeNPs and the hydroxyl-rich PVA matrix. The spectroscopic results support the incorporation of the SeNPs into PVA without major changes in their characteristic UV–Vis absorption.

3.2. Morphological and Colloidal Characterization of SeNPs@PVA89

Transmission electron microscopy (TEM) showed that the biogenic SeNPs exhibited a predominantly quasi-spherical morphology with a relatively narrow size distribution (Figure 2A,B). A total of 102 individual nanoparticles were measured, giving particle diameters ranging from 11 to 23 nm, with a mean diameter of 14.77 ± 2.47 nm and a median of 14.0 nm. The size distribution was centered around the median value and was adequately described by a Gaussian fit. Small cluster-like assemblies were occasionally observed; however, extensive particle coalescence was not evident in the analyzed micrographs.

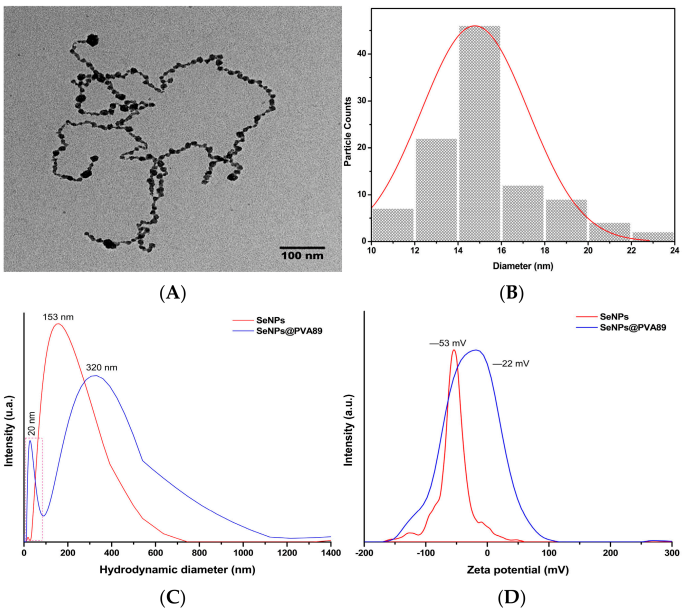


Figure 2. Morphological and dispersion characterization of biogenic SeNPs and SeNPs@PVA89. (**A**) Representative TEM micrograph showing the quasi-spherical morphology of the biogenic SeNPs; scale bar = 100 nm. (**B**) Particle-size distribution of biogenic SeNPs determined from TEM micrographs (n = 102), showing a mean diameter of 14.77 ± 2.47 nm and a Gaussian fit to the size distribution. (**C**) Hydrodynamic diameter of free SeNPs and SeNPs@PVA89 determined by DLS. (**D**) ζ-potential of free SeNPs and SeNPs@PVA89.

This behavior is likely attributable to attractive interparticle forces, including van der Waals interactions, as well as to the adsorption of phytochemicals and other biomolecules, such as proteins and polysaccharides, derived from the *A. glaucum* extract used during synthesis. These surface-associated biomolecules act as natural capping and stabilizing agents,

providing steric and electrostatic stabilization while limiting uncontrolled nanoparticle aggregation [28,29].

Despite these small assemblies, we observed no evidence of extensive aggregation or particle coalescence, indicating that the biosynthetic process yielded biogenic SeNPs with a morphology suitable for homogeneous incorporation into the PVA matrix.

The particle size determined by TEM differed considerably from the hydrodynamic diameter obtained by dynamic light scattering (DLS). Free biogenic SeNPs exhibited a hydrodynamic diameter of approximately 153 nm, which increased to approximately 320 nm after incorporation into PVA (Figure 2C). This difference is expected because DLS measures the hydrodynamic size of dispersed particles, including the nanoparticle surface and its associated hydrated layer. In biogenic SeNPs, this interfacial region may contain surface-associated phytochemicals, whereas after incorporation into PVA, it may also include hydrated polymer chains. Therefore, the larger DLS-derived diameter of SeNPs@PVA89 does not represent an increase in the primary particle size observed by TEM [30,31].

The ζ-potential also changed after incorporation into the polymer matrix, decreasing in magnitude from approximately −53 mV for free SeNPs to −22 mV for SeNPs@PVA89 (Figure 2D). This change is consistent with partial shielding of negatively charged surface groups by the PVA matrix [32]. Since PVA is a non-ionic polymer, the lower magnitude of the ζ-potential does not necessarily indicate a loss of colloidal stability. The hydrated polymer environment may instead contribute to steric stabilization of the nanoparticles and modify the relative contribution of electrostatic interactions to their dispersion behavior [33].

The simultaneous increase in hydrodynamic diameter and decrease in ζ-potential magnitude indicate a change in the incorporation into PVA [34,35]. These observations are consistent with the FTIR results, which showed changes in the hydrogen-bonding environment of the PVA hydroxyl groups and in several bands associated with the polymer chains. The DLS and ζ-potential measurements therefore provide additional evidence of an altered nanoparticle–polymer interface after incorporation into PVA, while the TEM results indicate that the primary particle size and overall morphology of the SeNPs were retained [36–39].

3.3. Morphological Characterization of SeNPs@PVA89 by SEM

Scanning electron microscopy revealed that the lyophilized SeNPs@PVA89 nanocomposite exhibited a porous three-dimensional morphology with interconnected cavities and lamellar-like regions (Figure 3A). This architecture is consistent with structures generated during freeze-drying, where ice-crystal formation and subsequent sublimation produce voids within the polymer matrix [40]. The observed morphology therefore primarily reflects the processing history of the nanocomposite rather than the intrinsic morphology of the individual nanoparticles [41]. The EDS spectrum confirmed the presence of selenium in the nanocomposite, together with the carbon and oxygen signals characteristic of the PVA matrix (Figure 3B).

Elemental mapping showed that the selenium signal was distributed throughout the analyzed regions of the PVA matrix, with no obvious localized enrichment (Figure 3C). This relatively homogeneous distribution supports effective incorporation of SeNP-associated material within the polymer network after mixing and freeze-drying. Our group previously reported a comparable distribution pattern in guar gum-based nanocomposites containing biogenic SeNPs, where EDS mapping also showed a broadly homogeneous selenium distribution throughout the polymeric matrix [6]. Together with the spectroscopic and dispersion analyses, these findings indicate that the preparation process enabled incorporation of biogenic SeNPs throughout the PVA-based nanocomposite while preserving a relatively uniform elemental distribution.

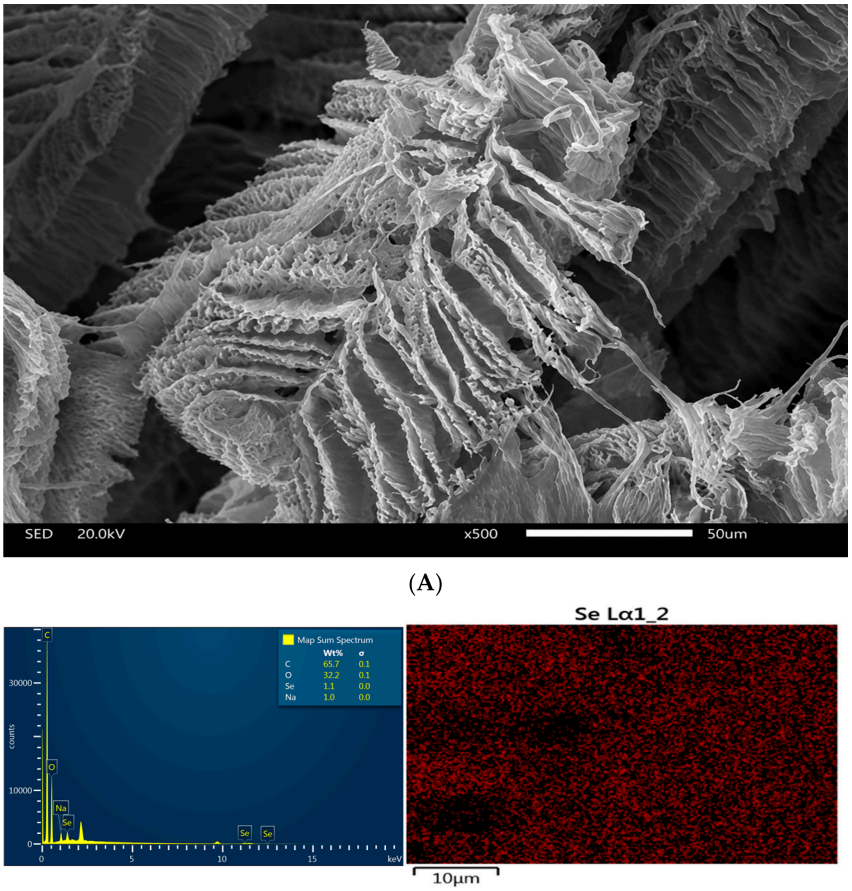
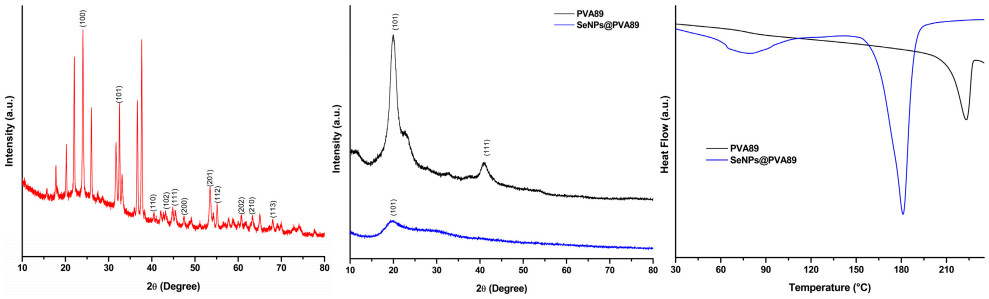


Figure 3. Morphological characterization and elemental analysis of SeNPs@PVA89 by scanning electron microscopy (SEM) and energy-dispersive X-ray spectroscopy (EDS). (**A**) Representative SEM micrograph showing the porous morphology of the lyophilized NC; (**B**) corresponding EDS spectrum; (**C**) EDS elemental mapping displaying the homogeneous distribution of selenium (red) throughout the polymeric matrix, supporting a relatively homogeneous distribution of selenium throughout the analyzed regions of the polymer matrix.

3.4. Structural and Thermal Changes Induced by SeNPs Incorporation into PVA

X-ray diffraction analysis confirmed the crystalline nature of the biogenic SeNPs and revealed structural changes in the PVA matrix after nanocomposite formation (Figure 4A,B). Free SeNPs showed diffraction peaks characteristic of crystalline elemental selenium, consistent with JCPDS card No. 06-0362 and previous reports on plant-mediated selenium nanoparticles [42,43]. Analysis of the diffraction peaks of the SeNPs indicated a monoclinic unit cell with parameters a = 4.9046 Å, b = 9.9897 Å, c = 6.8598 Å, and β = 90.26°.

The diffraction pattern of PVA89 showed a characteristic semicrystalline reflection centered at 19.9320°, corresponding to a *d*-spacing of 4.4510 Å, the (101) crystal plane, and ordered packing of PVA chains stabilized by intermolecular hydrogen bonding [43]. Moreover, we detected two other XRD peaks at 22.9369° and 41.0424°, indexed to the (200) and (111) crystal planes, corresponding to *d*-spacings of 3.8742 Å and 2.1974 Å, respectively. After incorporating SeNPs, the intensity of this reflection decreased, while the secondary reflection near 40.9° became markedly attenuated or was no longer clearly resolved. These changes indicate reduced crystalline organization in the polymer matrix after nanocomposite formation [44].



(**A**) (**B**) (**C**)

Figure 4. Structural and thermal characterization of biogenic SeNPs and the SeNPs@PVA89. (**A**) XRD pattern of biogenic SeNPs showing the characteristic reflections of crystalline selenium. (**B**) XRD patterns of PVA89 and SeNPs@PVA89, showing reduced peak intensity at approximately 19.9° and 40.9° after nanoparticle incorporation. (**C**) DSC thermograms of PVA89 and SeNPs@PVA89 show changes in the NC thermal transition profile.

The decrease in diffraction intensity is consistent with disruption of regular PVA chain packing by the incorporated nanoparticles and their associated surface species. Rather than indicating a loss of structural integrity, this behavior suggests a redistribution of polymer-chain organization around the nanoparticle interface. Similar reductions in crystalline order have been reported in PVA-based nanocomposites when nanoparticles interfere with hydrogen-bonded polymer-chain packing [44–46].

Differential scanning calorimetry supported the structural changes observed by XRD (Figure 4C). PVA89 exhibited a melting transition at approximately 223 °C, whereas SeNPs@PVA89 showed a lower melting transition near 180 °C. This decrease indicates that incorporating SeNPs altered the polymer matrix's thermal organization and reduced the stability of crystalline domains [47].

Changes in melting behavior after nanoparticle incorporation have been associated with disrupted intermolecular interactions and less regular polymer-chain packing in PVA-based nanocomposites [45–48]. In the present system, the lower melting transition is consistent with the FTIR and XRD results, which together indicate a modified hydrogen-bonding environment and reduced crystalline order after PVA interacts with the biogenic SeNPs.

Taken together, the XRD and DSC results indicate that incorporating biogenic SeNPs affects PVA's structural organization without eliminating the characteristic features of the polymer matrix. These changes are consistent with the formation of a nanoparticle–polymer interfacial region in which PVA chain packing is partially disrupted, supporting spectroscopic evidence of interaction between the hydroxyl-rich polymer and the surface-associated groups of the biogenic SeNPs.

3.5. Concentration-Dependent Effect of SeNPs@PVA89 on HDF Metabolic Activity

After physicochemical characterization, we evaluated the biological performance of SeNPs@PVA89 using complementary in vitro assays to assess its effects on fibroblast metabolic activity, cell migration, cytoskeletal organization, and intrinsic fluorescence. These assays were selected to assess the principal functional parameters commonly used in the biological evaluation of biomaterials before ultrastructural analysis.

3.6. MTT Assay

The effect of SeNPs@PVA89 on HDF metabolic activity was evaluated after 24 h of exposure using the MTT assay (Figure 5). A clear concentration-dependent response was observed. At 3 and 6 µg/mL, metabolic activity remained comparable to that of untreated controls, with mean values of approximately 100% and 99%, respectively, and no significant

differences between these groups. In contrast, exposure to concentrations of 12 µg/mL and above resulted in a marked decrease in metabolic activity.

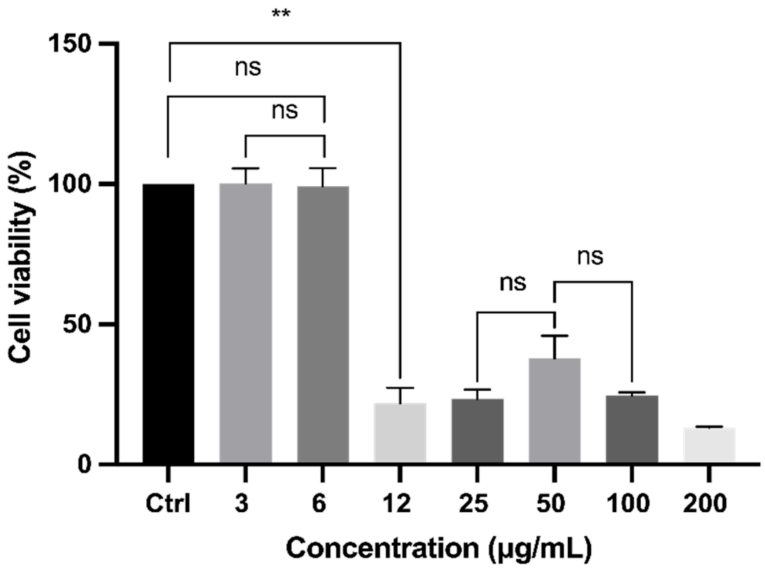


Figure 5. Dose-dependent effect of SeNPs@PVA89 on the metabolic activity of primary human dermal fibroblasts (HDF), as determined by the MTT assay after 24 h of exposure. Data are presented as mean ± SD ($n = 3$ independent biological replicates). Statistical analysis was performed using repeated-measures one-way ANOVA with the Geisser–Greenhouse correction, followed by Tukey's multiple-comparisons test. For clarity, only selected comparisons with the untreated control are indicated in the graph: ** $p < 0.01$, ns = not significant.

Specifically, metabolic activity decreased to approximately 22% at 12 µg/mL, 23% at 25 µg/mL, 38% at 50 µg/mL, 24% at 100 µg/mL, and 13% at 200 µg/mL. The 3 and 6 µg/mL groups differed significantly from all concentrations ≥12 µg/mL. In contrast, most comparisons among the higher-concentration groups were not significant, suggesting that metabolic activity fell into a low-response range once the threshold between 6 and 12 µg/mL was exceeded.

This concentration-dependent behavior is consistent with previous reports describing a biphasic biological response to SeNPs exposure, in which low concentrations are generally better tolerated. In contrast, higher concentrations are associated with reduced cellular metabolic activity and cytotoxic responses [49–52]. Previous studies in human dermal and gingival fibroblasts have likewise reported preserved cellular function at low SeNPs concentrations and a progressive decline at higher doses. However, the exact threshold varies by nanoparticle size, synthesis route, surface chemistry, stabilizing agents, and cell type [50–52].

These findings indicate that stabilization within PVA did not eliminate the characteristic concentration-dependent response of the biogenic SeNPs formulation. Under the conditions evaluated, 3 and 6 µg/mL preserved HDF metabolic activity, whereas concentrations ≥12 µg/mL produced a pronounced reduction. Based on these results, 3 µg/mL was selected for subsequent cellular imaging and ultrastructural analyses because it represented the lowest tested concentration with preserved metabolic activity and was also used to assess whether subcellular changes could occur in the absence of overt functional impairment.

3.7. Concentration-Dependent Effect of SeNPs@PVA89 on HDF Wound Closure

The effect of SeNPs@PVA89 on HDF wound closure was evaluated after 24 and 48 h of exposure relative to the initial scratch (T0) (Figure 6). We observed a clear concentration-

and time-dependent response. After 24 h, treatment with 3 µg/mL did not significantly affect wound closure compared with untreated controls. Although cultures exposed to 25 µg/mL also showed a reduction in the cell-free area at this time point, interpreting wound closure at concentrations above 3 µg/mL requires considering the marked reduction in metabolic activity observed in the MTT assay.

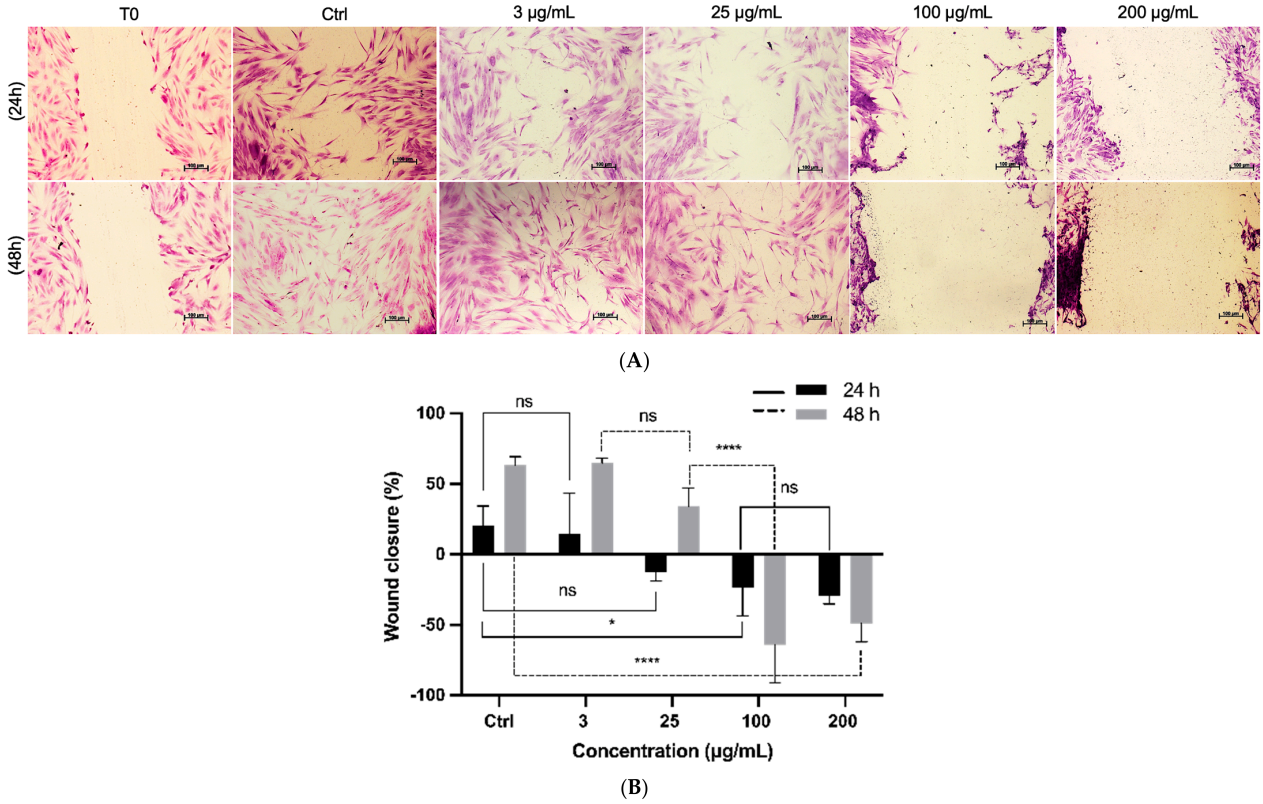


Figure 6. Concentration-dependent effect of SeNPs@PVA89 on fibroblast wound closure evaluated by the scratch assay after 24 and 48 h of exposure. (**A**) Representative micrographs of the scratched monolayer immediately after scratching (T0) and at 24 and 48 h. (**B**) Quantitative analysis of wound closure at 24 h and 48 h. Data are presented as mean ± SD ($n = 3$ independent biological replicates). Statistical analysis was performed using two-way ANOVA followed by Tukey's multiple-comparisons test. * $p < 0.05$, **** $p < 0.0001$. ns = not significant.

At 48 h, HDF exposed to 3 µg/mL continued to close the scratch progressively while maintaining an apparently intact surrounding monolayer. In contrast, cultures treated with 25 µg/mL showed areas of cell detachment despite a visible reduction in the scratch area. At 100 and 200 µg/mL, pronounced disruption of the monolayer was evident, with loss of the characteristic spindle-shaped morphology, cellular contraction, and extensive detachment. Under these conditions, changes in the remaining cell-free area cannot be interpreted as a direct measure of migratory capacity because cell loss substantially alters the wound-region geometry.

This distinction matters because the in vitro scratch assay does not measure cell migration alone. Wound closure results from the combined contributions of cell migration, proliferation, and survival, particularly over prolonged incubation periods [53]. Accordingly, the impaired or unstable closure observed at higher SeNPs@PVA89 concentrations is more consistent with fewer and less-intact HDFs available to repopulate the scratched area than with isolated inhibition of cellular migration.

This concentration dependence aligns with previous studies showing that selenium-based nanomaterials' effects on wound-related cellular responses vary markedly with

nanoparticle concentration, formulation, stabilizing matrix, and cell type [54–61]. For example, selenium-containing systems designed for controlled delivery have been reported to enhance wound closure under specific experimental conditions. Nejati et al. observed enhanced fibroblast migration in a HAMA/GelMA hydrogel containing SeNPs [58]. Other studies have also reported improved wound closure in keratinocyte or macrophage models exposed to SeNP formulations [60,61]. However, these findings should not be directly extrapolated to the present system because nanoparticle presentation and selenium bioavailability differ substantially among formulations.

In the present study, SeNPs@PVA89 at 3 μg/mL preserved both HDF metabolic activity and wound-closure behavior, whereas higher concentrations were associated with progressive loss of cellular integrity. These complementary findings support selecting 3 μg/mL for subsequent cytoskeletal and ultrastructural analyses, allowing cellular responses to be examined under an exposure condition in which conventional functional endpoints remained largely preserved.

3.8. Confocal Microscopy and F-Actin Organization

To determine whether exposure to a functionally tolerated concentration of SeNPs@PVA89 induced detectable changes in cellular architecture, HDF were examined after 24 h of exposure to 3 μg/mL of the nanocomposite (Figure 7). Epifluorescence microscopy showed that treated cells largely retained the characteristic spindle-shaped morphology observed in untreated controls, with preserved nuclear morphology and an overall F-actin organization comparable to that of control HDF. No widespread disruption of actin filaments, loss of cell spreading, or severe alterations in cellular architecture were evident under these conditions.

A limited number of treated cells exhibited thinner cytoplasmic extensions and subtle local variations in F-actin organization. Because these changes were qualitative and not observed across the cell population, they should be interpreted cautiously and do not provide evidence of a generalized cytoskeletal response. Overall, the preservation of HDF morphology and F-actin architecture is consistent with the MTT and wound-closure results obtained at 3 μg/mL.

Previous studies have also reported preserved fibroblast morphology and cytoskeletal organization after exposure to low concentrations of biogenic SeNPs. Tritean et al. observed maintained morphology and F-actin organization in primary human dermal fibroblasts exposed to 2.5 μg/mL biogenic SeNPs [50]. More generally, maintaining an organized actin cytoskeleton is associated with preserved cell spreading and functional interactions with biomaterial surfaces [62].

Confocal microscopy revealed discrete punctate fluorescent structures distributed throughout the cytoplasm of HDF exposed to 3 μg/mL SeNPs@PVA89, predominantly localized perinuclearly, whereas comparable punctate signals were not detected in untreated controls (Figure 7C,D). These fluorescent structures were observed in cells with preserved overall F-actin organization, indicating that the intracellular fluorescent signal was not accompanied by overt disruption of the actin cytoskeleton.

We further evaluated the nanosystem's intrinsic fluorescence without exogenous fluorophores (Figure 8). Untreated HDF did not exhibit detectable autofluorescence under the imaging conditions employed, whereas SeNPs@PVA89-exposed cells displayed punctate fluorescence in the green (Figure 8A), red (Figure 8B), and blue (Figure 8C) spectral channels. The merged intracellular pattern was predominantly cytoplasmic and was consistent with the discrete fluorescent structures observed in Figure 7.

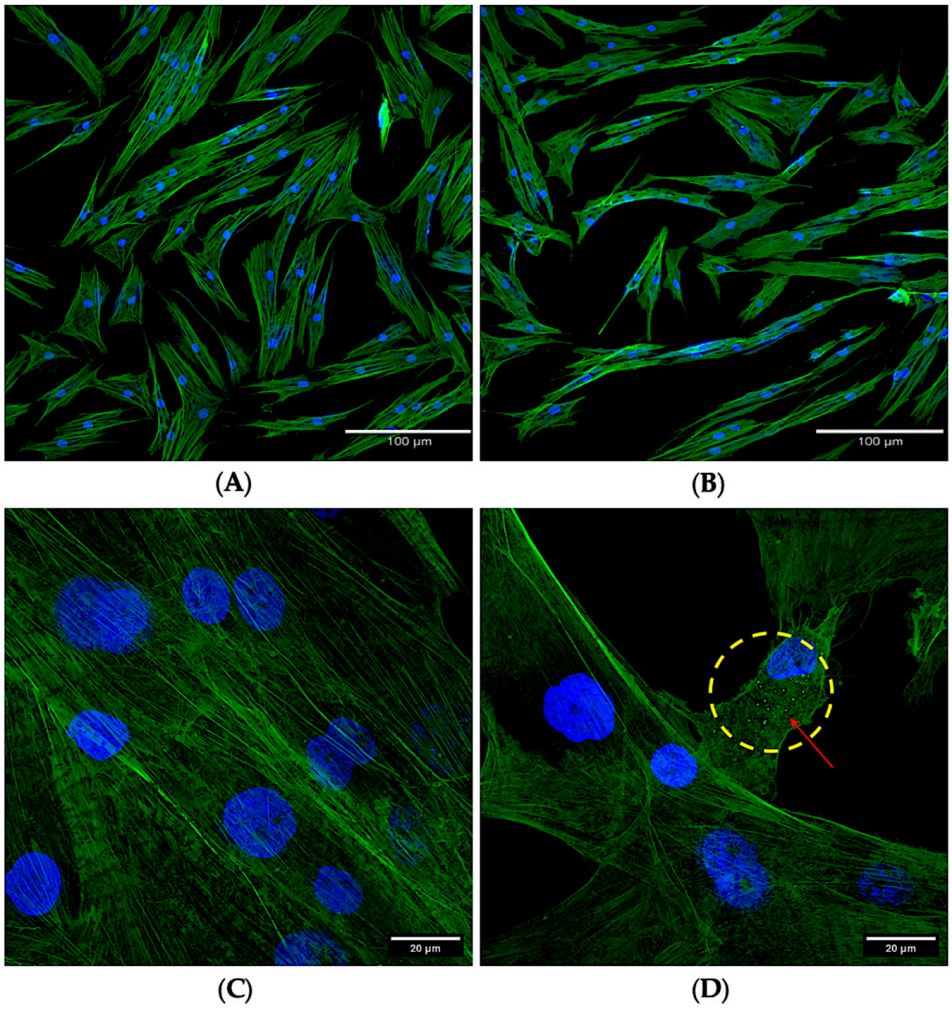
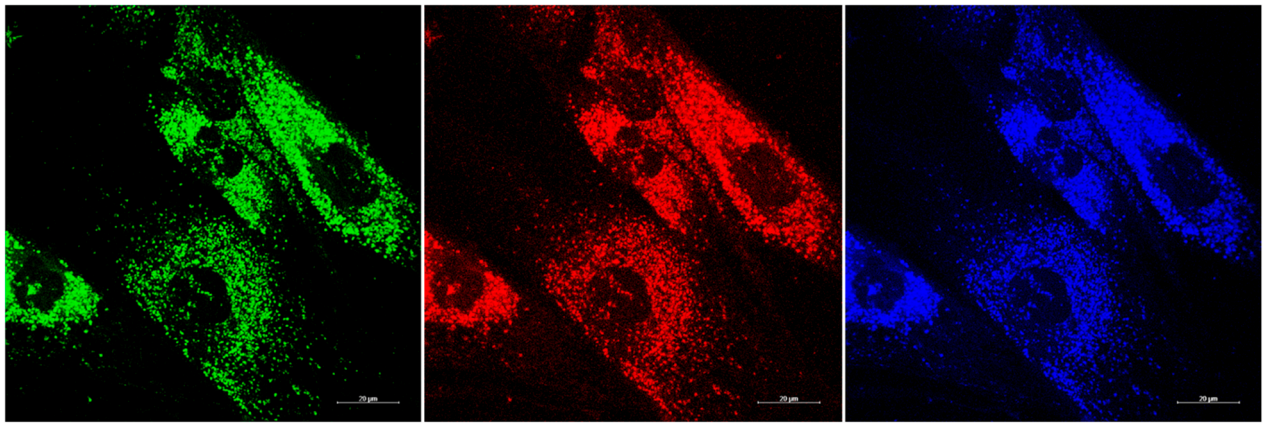


Figure 7. Effect of SeNPs@PVA89 on fibroblast morphology and F-actin organization after 24 h of exposure. (**A**) Untreated control fibroblasts and (**B**) fibroblasts exposed to 3 µg/mL of the NC, observed by epifluorescence microscopy after staining with phalloidin (F-actin, green) and DAPI (nuclei, blue). (**C**) Confocal image of untreated fibroblasts showing normal F-actin organization. (**D**) Confocal image of fibroblasts exposed to 3 µg/mL of the NC, showing preserved F-actin organization and discrete punctate intracellular fluorescent structures predominantly distributed within the cytoplasm. The arrow and yellow circle indicate changes observed in the treated cells (scale bar, 20 µm).

Intrinsic fluorescence has been reported for selenium-based nanosystems and may depend on particle size, crystallinity, synthesis route, and surface chemistry [63–67]. In the present formulation, biomolecules adsorbed on the SeNP surface during biogenic synthesis may also influence the multichannel fluorescence. The PVA matrix likely contributes primarily by maintaining the physicochemical environment and nanoparticle dispersion rather than acting as the fluorophore itself. This interpretation is consistent with the spectroscopic, DLS, ζ-potential, XRD, and DSC results, which together indicate interaction between the SeNPs surface and the PVA matrix.

Although the punctate fluorescence is compatible with intracellular association of SeNPs@PVA89, fluorescence microscopy alone does not establish the elemental identity of the fluorescent structures or definitively demonstrate intracellular selenium localization. Therefore, we interpreted the fluorescence findings alongside TEM observations to assess the intracellular fate and ultrastructural response of HDF exposed to the nanocomposite.

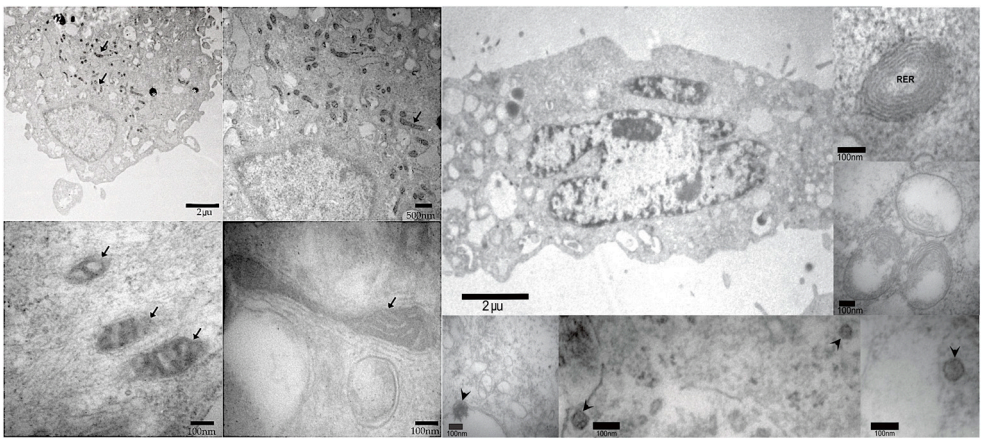


(**A**) (**B**) (**C**)

Figure 8. Intrinsic multichannel fluorescence of SeNPs@PVA89 in HDF after 24 h of exposure. Confocal images were acquired without exogenous fluorescent probes. Fluorescence associated with SeNPs@PVA89 was detected in the (**A**) green, (**B**) red, and (**C**) blue spectral channels, showing a punctate intracellular distribution predominantly within the cytoplasm. Untreated HDF did not exhibit detectable autofluorescence under the same imaging conditions. Images were processed using identical settings for comparison.

3.9. Ultrastructural Response of HDF to SeNPs@PVA89

Transmission electron microscopy revealed clear ultrastructural differences between untreated HDF and cells exposed to 3 µg/mL SeNPs@PVA89 for 24 h (Figure 9). Untreated cells maintained normal nuclear morphology, elongated mitochondria with well-defined cristae, a normally organized rough endoplasmic reticulum (RER), and occasional lipid droplets (Figure 9A). In contrast, treated HDF showed mitochondrial fragmentation, disrupted cristae architecture, dilated and rearranged RER cisternae, and concentric membrane structures. An increased number of membrane-bound cytoplasmic vesicular compartments was also observed (Figure 9B).



(**A**) (**B**)

Figure 9. Transmission electron microscopy (TEM) of human dermal fibroblasts after 24 h of exposure to SeNPs@PVA89. (**A**) Untreated control fibroblast showing a well-preserved ultrastructure, including elongated mitochondria (arrow) and occasional lipid droplets (*). (**B**) Fibroblast exposed to 3 µg/mL of SeNPs@PVA89, showing ultrastructural alterations in fibroblasts, characterized by abundant vacuoles, rough endoplasmic reticulum (RER), and mitochondria. Different stages of nanoparticle internalization by fibroblasts are shown, with the nanoparticles appearing as electron-dense structures (arrowheads).

Electron-dense structures were detected within some of these membrane-bound compartments. Their morphology was compatible with nanoparticle-associated material; however, their elemental composition was not directly confirmed. Therefore, these observations should be interpreted as morphological evidence consistent with intracellular association and vesicular sequestration rather than as definitive proof of intracellular selenium localization [63].

Similar intracellular compartmentalization of functionalized SeNPs has been reported in endosomal-, lysosomal-, and mitochondria-associated regions [68–70]. Bissardon et al. [68], showed that functionalized SeNPs, at sub-toxic concentrations, accumulated in lysosome-related organelles and associated with mitochondrial regions in prostate cancer cells. Although that study used a different cellular model, it supports the idea that SeNP-containing systems may remain intracellularly compartmentalized under exposure conditions that do not immediately cause extensive cell death.

The mitochondrial and RER alterations observed in the present study are also consistent with previous reports identifying these organelles as early targets of nanoparticle-induced cellular stress [69–73]. In particular, SeNPs exposure has been associated with mitochondrial dysfunction, altered redox homeostasis, and endoplasmic reticulum stress (ER stress) in different experimental models [70–74]. Moreover, multiple cytotoxic mechanisms induced by selenium compounds have been described, including glycolysis inhibition, microtubule depolymerization, autophagy inhibition, ROS generation, induction of caspase-dependent and -independent apoptosis, cell cycle arrest, ER stress, and DNA damage [75,76]. However, we did not directly measure these mechanisms; therefore, the present TEM findings should be interpreted as ultrastructural evidence of organelle remodelling rather than proof of a specific molecular pathway.

Importantly, the ultrastructural alterations detected at 3 μg/mL, namely mitochondrial fragmentation, cristae disruption, RER remodeling, and membrane-bound vesicular compartments containing electron-dense structures, occurred under the same exposure conditions in which HDF metabolic activity, wound-closure behavior, and overall F-actin organization remained largely preserved. This divergence suggests that conventional cytocompatibility endpoints alone may not capture the full cellular response to SeNPs@PVA89 and supports ultrastructural analysis as a useful complement to functional assays for understanding the nano–bio interactions of PVA-stabilized SeNPs.

From a tissue-engineering perspective, this distinction matters because biomaterials for regenerative applications should not only preserve cell viability and gross functional behavior but also maintain cellular homeostasis at the subcellular level. The present findings therefore support a more comprehensive evaluation strategy for nanoparticle-containing biomaterials, in which ultrastructural assessment complements conventional cytocompatibility assays to define biologically better-tolerated conditions for future tissue-engineering applications.

The original contribution of this study goes beyond the development of a redispersible formulation of biogenic SeNPs stabilized with PVA. By integrating physicochemical characterization with functional, fluorescence, and ultrastructural analyses in human dermal fibroblasts, it shows that a nanocomposite may appear cytocompatible under conventional assays and still induce ultrastructural alterations detectable by TEM. In addition, the intrinsic fluorescence of the nanocomposite, possibly influenced by precursor chemistry and the phytochemical composition of the plant extract, enabled confocal visualization of punctate intracellular signals that, together with the TEM observations, provided a more comprehensive characterization of the cellular interactions with SeNPs@PVA89.

4. Conclusions

Biogenic SeNPs synthesized using *A. glaucum* extract were successfully stabilized within a medium-molecular-weight PVA matrix, preserving their nanoscale characteristics

and characteristic optical response while altering the physicochemical environment of the polymer–nanoparticle system. Spectroscopic, dispersion, structural, thermal, and elemental analyses supported the formation of SeNPs@PVA89, with changes in hydrodynamic behavior, surface potential, polymer-chain organization, and crystalline structure consistent with interactions between the biogenic nanoparticle surface and the PVA matrix.

The biological response of HDF was strongly concentration-dependent. At 3 and 6 μg/mL, metabolic activity remained preserved, whereas concentrations ≥12 μg/mL produced a marked decrease in the MTT response. At 3 μg/mL, HDFs also maintained wound closure, overall morphology, and F-actin organization. Nevertheless, confocal microscopy revealed discrete intracellular fluorescence, while TEM showed mitochondrial fragmentation, altered cristae, RER remodelling, and membrane-bound vesicular compartments containing electron-dense structures. Although we did not directly confirm the elemental identity of these intracellular structures, their morphology was consistent with intracellular association and vesicular sequestration of the nanosystem.

These findings show that meeting conventional cytocompatibility endpoints does not necessarily rule out a subcellular response. The ultrastructural alterations detected under functionally tolerated exposure conditions provide additional biological information that complements metabolic, wound-closure, and cytoskeletal assays. Although we did not directly investigate the underlying mechanisms, the mitochondrial and RER alterations observed here may represent a cellular stress response preceding overt functional impairment.

From a tissue-engineering perspective, this distinction matters because biomaterials intended for regenerative applications should be evaluated not only for cell viability and gross functional behaviour, but also for their effects on subcellular organisation. SeNPs@PVA89 therefore provides a useful model for examining how polymer-stabilized biogenic nanoparticles interact with normal human fibroblasts. At the same time, the combined physicochemical, functional, fluorescence, and ultrastructural approach used here offers a more comprehensive basis for evaluating nanoparticle-containing biomaterials intended for future regenerative applications.

Author Contributions: Conceptualization, C.V., Z.Y.G.-C., S.G.-M., B.I.D.S.-T. and J.A.H.-D.; methodology, J.A.H.-D., B.I.D.S.-T., E.B.B.-A., R.O.-H., A.G.-B.; software, J.A.H.-D., B.I.D.S.-T., E.B.B.-A., R.O.-H. and C.V.; validation, C.V., Z.Y.G.-C., M.M.-V. and J.A.H.-D.; formal analysis, J.A.H.-D., Z.Y.G.-C. and C.V.; investigation, J.A.H.-D., B.I.D.S.-T., E.B.B.-A., R.O.-H., A.G.-B. and Z.Y.G.-C.; resources, Z.Y.G.-C., C.V., S.G.-M., M.M.-V., R.O.-H. and S.M.N.-D.; data curation, J.A.H.-D., B.I.D.S.-T., C.V. and Z.Y.G.-C.; writing—original draft preparation, J.A.H.-D., B.I.D.S.-T., C.V., R.O.-H. and Z.Y.G.-C.; writing—review and editing, J.A.H.-D., C.V., and Z.Y.G.-C.; visualization, J.A.H.-D., B.I.D.S.-T., C.V. and Z.Y.G.-C.; supervision, C.V., Z.Y.G.-C.; project administration, C.V., Z.Y.G.-C., S.G.-M. and M.M.-V.; funding acquisition, C.V., Z.Y.G.-C., S.G.-M. and M.M.-V. All authors have read and agreed to the published version of the manuscript.

Funding: This research was partially funded by Secretaría de Ciencia, Humanidades, Tecnología e Innovación (SECIHTI), grant number CBF2023-2024-2164; Centro de Investigación y Asistencia en Tecnología y Diseño del Estado de Jalisco (CIATEJ), PITs 2025, grant number 1005100008; and Consejo Estatal de Ciencia y Tecnología de Jalisco (COECyTJAL), Mexico, through the Jalisco–Québec Bilateral Cooperation Program in Science, Technology, and Innovation 2026, Project No. 12120.

Data Availability Statement: The data that support the findings of the study are available from the corresponding authors upon reasonable request.

Acknowledgments: We thank SECIHTI–Mexico for the awarded doctoral scholarship (No. 717214) and for the use of the SINANOTOX laboratory (National Nanotoxicological Evaluation System) at CIATEJ, A.C.

Conflicts of Interest: The authors declare no conflicts of interest.

References

1. Ferro, C.; Florindo, H.F.; Santos, H.A. Selenium Nanoparticles for Biomedical Applications: From Development and Characterization to Therapeutics. *Adv. Healthc. Mater.* **2021**, *10*, e2100598. [CrossRef]
2. El-Saadony, M.T.; Saad, A.M.; Alkafaas, S.S.; Dladla, M.; Ghosh, S.; Mohammed, D.M.; Soliman, T.N.; Elkelish, A.; Kha-lil, F.M.A.; Fahmy, M.A.; et al. Selenium Nanoparticles: Eco-Friendly Synthesis, Biological Activities and Biomedical Applications—A Comprehensive Review. *Mater. Today Bio* **2026**, *37*, 102946. [CrossRef]
3. Zhang, Y.; Qin, X.; Wan, Z.; Deng, C.; Deng, T. Selenium Nanoparticles: Biomedical Application Advances and New Sto-matology Pathways. *Int. J. Nanomed.* **2025**, *20*, 16027–16053. [CrossRef]
4. Qamar, N.; Poimala, M.; Jäntti, J.; Das Gupta, S.; Hawash, A.; Leelarathne, C.S.; Mennerich, D.; Dufour, A.; Mäkelä, J.T.A.; Åström, P.; et al. Selenium Nanoparticles as Antioxidants: Green Synthesis, Characterization, and Evaluation of Bioactivity. *Biomater. Sci.* **2026**, *14*, 2317–2333. [CrossRef]
5. Garza-García, J.J.O.; Hernández-Díaz, J.A.; León-Morales, J.M.; Velázquez-Juárez, G.; Zamudio-Ojeda, A.; Arratia-Quijada, J.; Reyes-Maldonado, O.K.; López-Velázquez, J.C.; García-Morales, S. Selenium Nanoparticles Based on Amphipterygium glaucum Extract with Antibacterial, Antioxidant, and Plant Biostimulant Properties. *J. Nanobiotechnol.* **2023**, *21*, 252. [CrossRef]
6. Hernández-Díaz, J.A.; Arias-García, A.A.; Gutiérrez-Becerra, A.; Comas-García, M.; Vázquez-Lepe, M.O.; Hernández-Cristóbal, O.; García-Morales, S.; Martínez-Velázquez, M.; García-Carvajal, Z.Y. Development and Characterization of a Guar Gum Bionanocomposite Loaded with Biogenic Selenium Nanoparticles and Its Cytotoxic Evaluation. *Gels* **2026**, *12*, 376. [CrossRef]
7. Ying, S.; Guan, Z.; Ofoegbu, P.C.; Clubb, P.; Rico, C.; He, F.; Hong, J. Green Synthesis of Nanoparticles: Current Developments and Limitations. *Environ. Technol. Innov.* **2022**, *26*, 102336. [CrossRef]
8. Shahzadi, S.; Fatima, S.; ul Ain, Q.; Shafiq, Z.; Janjua, M.R.S.A. A Review on Green Synthesis of Silver Nanoparticles (SNPs) Using Plant Extracts: A Multifaceted Approach in Photocatalysis, Environmental Remediation, and Biomedicine. *RSC Adv.* **2025**, *15*, 3858–3903. [CrossRef]
9. Jailani, A.; Hidzer, M.H.; Firdaus, A.H.M.; Sapuan, S.M.; Zainudin, E.S.; Atiqah, A.; Wan Jaafar, W.M.; Suryanegara, L. Enhancing Polyvinyl Alcohol (PVA) Nanocomposites: Key Properties, Applications and Challenges in Advanced Engineering. *Def. Technol.* **2026**, *55*, 11–29. [CrossRef]
10. Iravani, S. Green Synthesis of Metal Nanoparticles Using Plants. *Green Chem.* **2011**, *13*, 2638. [CrossRef]
11. Bhiri, N.; Masquelez, N.; Nasri, M.; Nasri, R.; Hajji, M.; Li, S. Synthesis, Characterization, and Stability Study of Selenium Nanoparticles Coated with Purified Polysaccharides from Ononis Natrix. *Nanomaterials* **2025**, *15*, 435. [CrossRef]
12. Bhat, V.G.; Masti, S.P.; Narasagoudr, S.S.; Kurabetta, L.K.; Gunaki, M.N.; Hunashyal, A.A.; Chougale, R.B.; Malabadi, R.B. Antimicrobial Silver Nanoparticle-Doped Poly(Vinyl Alcohol)/Guar Gum/Gum Ghatti Nanocomposites: A Multi-faceted Step towards Sustainable Packaging. *Sustain. Food Technol.* **2026**, *4*, 3884–3899. [CrossRef]
13. Fadeel, B.; Farcal, L.; Hardy, B.; Vázquez-Campos, S.; Hristozov, D.; Marcomini, A.; Lynch, I.; Valsami-Jones, E.; Alenius, H.; Savolainen, K. Advanced Tools for the Safety Assessment of Nanomaterials. *Nat. Nanotechnol.* **2018**, *13*, 537–543. [CrossRef]
14. Akhtar, S.; Zuhair, F. Advancing Nanomedicine Through Electron Microscopy: Insights into Nanoparticle Cellular Interactions and Biomedical Applications. *Int. J. Nanomed.* **2025**, *20*, 2847–2878. [CrossRef]
15. Hernández-Díaz, J.A.; Arias-García, A.A.; García-Morales, S.; García-Carvajal, Z.Y.; Martínez-Velázquez, M. Aerogel de PVA Cargado Con Nanopartículas Biogénicas de Selenio: Propiedades Fisicoquímicas y Ensayos de Citotoxicidad. *Mundo Nano* **2025**, *19*, e69872. [CrossRef]
16. Gupta, B.; Bano, S.; Singh, R. High-Performance Silver Nanoparticles Embedded Conductive PVA Hydrogel for Stretchable Wearable Triboelectric Nanogenerators. *J. Power Sources* **2025**, *632*, 236271. [CrossRef]
17. Nitta, I.; Taguchi, I.; Chatani, Y. *Sen-I Kagaku Kenkyusho Nenpo (Annual Reports of Research Institute of Fiber Science)*; Osaka University: Osak, Japan, 1957; Volume 10, p. 1.
18. Muzata, T.S.; Gebrekrstos, A.; Orasugh, J.T.; Ray, S.S. An Overview of Recent Advances in Polymer Composites with Improved UV-Shielding Properties. *J. Appl. Polym. Sci.* **2023**, *140*, e53693. [CrossRef]
19. Chang, C.-C.; Lee, K.-M.; Huang, C.-H. The Optical Properties of Metal-Free Polymer Films with Self-Assembled Nanoparticles. *Polymers* **2021**, *13*, 4230. [CrossRef]
20. Mebed, A.M.; Mohsen, A.H.; Hassan, D.J.; Ali, N.A.; Hussein, S.I.; Noori, F.T.M.; Abd-Elnaiem, A.M.; Alraih, A.M.; Ab-delbaki, R.F. A Flexible, Antibacterial Platform: Silver-Tuned Polyvinyl Alcohol with Enhanced Opto-Mechanical and Electrical Properties. *Polymers* **2026**, *18*, 415. [CrossRef]
21. Farag, O.F.; El-Sayed, A.S.A.; Abdel-Fattah, E.M. One-Step Synthesis of Ag Nanoparticles Incorporated PVA Nanocomposite via Plasma Reduction Route. *Sci. Rep.* **2025**, *15*, 20103. [CrossRef]
22. Alghunaim, N.S. Optimization and Spectroscopic Studies on Carbon Nanotubes/PVA Nanocomposites. *Results Phys.* **2016**, *6*, 456–460. [CrossRef]

23. Soni, S.R.; Bhunia, B.K.; Kumari, N.; Dan, S.; Mukherjee, S.; Mandal, B.B.; Ghosh, A. Therapeutically Effective Controlled Release Formulation of Pirfenidone from Nontoxic Biocompatible Carboxymethyl Pullulan-Poly(Vinyl Alcohol) Interpenetrating Polymer Networks. *ACS Omega* **2018**, *3*, 11993–12009. [CrossRef]
24. Al-Marhaby, F.A.; Abdelkarim, A.; Seoudi, R. Exploring the Impact of Silver Nanoparticles on the Structure, Optical Properties, and Dielectric Response of PVA–PVP Blends. *Sci. Afr.* **2026**, *31*, e03120. [CrossRef]
25. Usawattanakul, N.; Torgbo, S.; Sukyai, P.; Khantayanuwong, S.; Puangsin, B.; Srichola, P. Development of Nanocompo-site Film Comprising of Polyvinyl Alcohol (PVA) Incorporated with Bacterial Cellulose Nanocrystals and Magnetite Nanoparticles. *Polymers* **2021**, *13*, 1778. [CrossRef]
26. Ortega-Sánchez, C.; Melgarejo-Ramírez, Y.; Rodríguez-Rodríguez, R.; Jiménez-Ávalos, J.A.; Giraldo-Gómez, D.M.; Gutiérrez-Gómez, C.; Rodríguez-Campos, J.; Luna-Bárcenas, G.; Velasquillo, C.; Martínez-López, V.; et al. Hydrogel Based on Chitosan/Gelatin/Poly(Vinyl Alcohol) for In Vitro Human Auricular Chondrocyte Culture. *Polymers* **2024**, *16*, 479. [CrossRef]
27. Mousa, M.; Dong, Y. The Role of Nanoparticle Shapes and Structures in Material Characterisation of Polyvinyl Alcohol (PVA) Bionanocomposite Films. *Polymers* **2020**, *12*, 264. [CrossRef]
28. Gentili, D.; Ori, G. Reversible Assembly of Nanoparticles: Theory, Strategies and Computational Simulations. *Nanoscale* **2022**, *14*, 14385–14432. [CrossRef]
29. Sidhu, A.K.; Verma, N.; Kaushal, P. Role of Biogenic Capping Agents in the Synthesis of Metallic Nanoparticles and Evaluation of Their Therapeutic Potential. *Front. Nanotechnol.* **2022**, *3*, 801620. [CrossRef]
30. Abdihaji, M.; Mirzaei Chegeni, M.; Hadizadeh, A.; Farrokhzad, N.; Kheradmand, Z.; Fakhrfatemi, P.; Faress, F.; Moeinabadi-Bidgoli, K.; Noorbazargan, H.; Mostafavi, E. Polyvinyl Alcohol (PVA)-Based Nanoniosome for Enhanced In Vitro Delivery and Anticancer Activity of Thymol. *Int. J. Nanomed.* **2023**, *18*, 3459–3488. [CrossRef]
31. Mahmoudi, M.; Lynch, I.; Ejtehadi, M.R.; Monopoli, M.P.; Bombelli, F.B.; Laurent, S. Protein−Nanoparticle Interactions: Opportunities and Challenges. *Chem. Rev.* **2011**, *111*, 5610–5637. [CrossRef]
32. Piacenza, E.; Presentato, A.; Ferrante, F.; Cavallaro, G.; Alduina, R.; Chillura Martino, D.F. Biogenic Selenium Nanoparticles: A Fine Characterization to Unveil Their Thermodynamic Stability. *Nanomaterials* **2021**, *11*, 1195. [CrossRef]
33. Cortés, H.; Hernández-Parra, H.; Bernal-Chávez, S.A.; Prado-Audelo, M.L.D.; Caballero-Florán, I.H.; Borbolla-Jiménez, F.V.; González-Torres, M.; Magaña, J.J.; Leyva-Gómez, G. Non-Ionic Surfactants for Stabilization of Polymeric Nano-particles for Biomedical Uses. *Materials* **2021**, *14*, 3197. [CrossRef]
34. Xin, Y.; Nagata, T.; Kato, K.; Xu, Y.; Shirai, T. Role of Polyvinylpyrrolidone in the Polyol Synthesis of Platinum Nanoparticles. *Nanoscale Adv.* **2024**, *6*, 3034–3040. [CrossRef]
35. Ali, S.A.; Konwar, A.N.; Thakur, D.; Kundu, S. Metal (Ag)/Metal Oxide (CuO, ZnO)@Polyvinyl Alcohol (PVA) Nano-composite Free-Standing Films: Physical and Antimicrobial Properties. *Surf. Interfaces* **2025**, *56*, 105587. [CrossRef]
36. Chen, X.; Wang, T. Preparation and Characterization of Atrazine-Loaded Biodegradable PLGA Nanospheres. *J. Integr. Agric.* **2019**, *18*, 1035–1041. [CrossRef]
37. Alabrahim, O.A.A.; Abdeldayem, A.M.; Azzazy, H.M.E.-S. Green Synthesis of Metallic Nanoparticles Using Pistacia Species: Improved Stability and Biological Activities. *Nanoscale Adv.* **2025**, *7*, 5449–5478. [CrossRef]
38. Singaravelu, S.; Motsoene, F.; Abrahamse, H.; Dhilip Kumar, S.S. Green-Synthesized Metal Nanoparticles: A Promising Approach for Accelerated Wound Healing. *Front. Bioeng. Biotechnol.* **2025**, *13*, 1637589. [CrossRef]
39. Cetin, A.; Ilk Capar, M. Functional-Group Effect of Ligand Molecules on the Aggregation of Gold Nanoparticles: A Molecular Dynamics Simulation Study. *J. Phys. Chem. B* **2022**, *126*, 5534–5543. [CrossRef]
40. Song, X.; Li, X.; Zhao, C.; Liang, L.; Guo, L.; Zhou, Y.; Zhu, B.; Peng, J. Structural and Performance Optimization of Environmentally Friendly Phenolic Resin/Polyvinyl Alcohol/Pure Terephthalic Acid/Silicone Carbide (PF/PVA/PTA/SiC) Porous Composite Grinding Wheels Prepared via Freeze-Drying Methodology. *Polymers* **2025**, *17*, 758. [CrossRef]
41. Ma, Y.; Wang, X.; Su, T.; Lu, F.; Chang, Q.; Gao, J. Recent Advances in Macroporous Hydrogels for Cell Behavior and Tissue Engineering. *Gels* **2022**, *8*, 606. [CrossRef]
42. Senthil Kumaran, C.K.; Agilan, S.; Velauthapillai, D.; Muthukumarasamy, N.; Thambidurai, M.; Senthil, T.S.; Bal-asundaraprabhu, R. Synthesis and Characterization of Selenium Nanowires. *ISRN Nanotechnol.* **2011**, *2011*, 589073. [CrossRef]
43. Souza, L.M.d.S.; Dibo, M.; Sarmiento, J.J.P.; Seabra, A.B.; Medeiros, L.P.; Lourenço, I.M.; Kobayashi, R.K.T.; Nakazato, G. Biosynthesis of Selenium Nanoparticles Using Combinations of Plant Extracts and Their Antibacterial Activity. *Curr. Res. Green Sustain. Chem.* **2022**, *5*, 100303. [CrossRef]
44. Hong, X.; Zou, L.; Zhao, J.; Li, C.; Cong, L. Dry-Wet Spinning of PVA Fiber with High Strength and High Young's Modulus. *IOP Conf. Ser. Mater. Sci. Eng.* **2018**, *439*, 042011. [CrossRef]
45. Pang, Y.; Zhang, N.; Liu, Y.; Zhang, J. High-Performance Biodegradable Poly(Vinyl Alcohol)/Starch Composites via Al-kaline-Regulated Crystalline Engineering. *Ind. Crops Prod.* **2024**, *220*, 119143. [CrossRef]
46. Yang, T.; Wu, J.; Yao, Y.; Wang, K.; Zhang, Q.; Fu, Q. Towards the Toughness-Strength Balance of Poly(Vinyl Alcohol) Films via Synergic Plasticization. *Polymer* **2024**, *301*, 127031. [CrossRef]

47. Chakraborty, S.; Lim, F.C.H.; Ye, J. Achieving an Optimal Tg Change by Elucidating the Polymer–Nanoparticle Interface: A Molecular Dynamics Simulation Study of the Poly(Vinyl Alcohol)–Silica Nanocomposite System. *J. Phys. Chem. C* **2019**, *123*, 23995–24006. [CrossRef]
48. Mbhele, Z.H.; Salemane, M.G.; van Sittert, C.G.C.E.; Nedeljković, J.M.; Djoković, V.; Luyt, A.S. Fabrication and Characterization of Silver−Polyvinyl Alcohol Nanocomposites. *Chem. Mater.* **2003**, *15*, 5019–5024. [CrossRef]
49. Varlamova, E.G.; Gudkov, S.V.; Plotnikov, E.Y.; Turovsky, E.A. Size-Dependent Cytoprotective Effects of Selenium Nanoparticles during Oxygen-Glucose Deprivation in Brain Cortical Cells. *Int. J. Mol. Sci.* **2022**, *23*, 7464. [CrossRef]
50. Tritean, N.; Dima, Ș.-O.; Trică, B.; Stoica, R.; Ghiurea, M.; Moraru, I.; Cimpean, A.; Oancea, F.; Constantinescu-Aruxandei, D. Selenium-Fortified Kombucha–Pollen Beverage by In Situ Biosynthesized Selenium Nanoparticles with High Bio-compatibility and Antioxidant Activity. *Antioxidants* **2023**, *12*, 1711. [CrossRef]
51. Tawgozy, F.H.A.; Mohammed, R.A.; Hamasalih, R.M.; Qadr, S.S.; Mala, S.F.; Mojarradgandoukmolla, S.; Abdulrahman, Z.F.A. Antimicrobial Potency and Biocompatibility of Biogenic Selenium Nanoparticles by Prosopis Farcta. *Microb. Pathog.* **2026**, *216*, 108495. [CrossRef]
52. Van Oeveren, W. Obstacles in Haemocompatibility Testing. *Scientifica* **2013**, *2013*, 392584. [CrossRef]
53. Molefe, P.F.; Ghasemishahrestani, Z.; Khumalo, N.P.; Bayat, A. The In Vitro Wound-Scratch Assay: Applications, Tech-nical Advances, and Limitations in Wound Healing Research. *Int. Wound J.* **2026**, *23*, e70964. [CrossRef]
54. Gorudko, I.V.; Grigorieva, D.V.; Gusakov, G.A.; Baran, L.V.; Reut, V.E.; Sak, E.V.; Baimler, I.V.; Simakin, A.V.; Dorokhov, A.S.; Izmailov, A.Y.; et al. Rod and Spherical Selenium Nanoparticles: Physicochemical Properties and Effects on Red Blood Cells and Neutrophils. *Biochim. Biophys. Acta Gen. Subj.* **2025**, *1869*, 130777. [CrossRef]
55. Rajkumar, K.; MVS, S.; Koganti, S.; Burgula, S. Selenium Nanoparticles Synthesized Using Pseudomonas Stutzeri (MH191156) Show Antiproliferative and Anti-Angiogenic Activity Against Cervical Cancer Cells. *Int. J. Nanomed.* **2020**, *15*, 4523–4540. [CrossRef]
56. Cao, J.; Zhang, Y.; Zhang, P.; Zhang, Z.; Zhang, B.; Feng, Y.; Li, Z.; Yang, Y.; Meng, Q.; He, L.; et al. Turning Gray Selenium into a Nanoaccelerator of Tissue Regeneration by PEG Modification. *Bioact. Mater.* **2022**, *15*, 131–144. [CrossRef]
57. Chen, Y.; Zhu, F.; Chen, J.; Liu, X.; Li, R.; Wang, Z.; Cheong, K.-L.; Zhong, S. Selenium Nanoparticles Stabilized by Sargas-sum Fusiforme Polysaccharides: Synthesis, Characterization and Bioactivity. *Int. J. Biol. Macromol.* **2024**, *269*, 132073. [CrossRef]
58. Nejati, O.; Tışlı, B.; Yaşayan, G.; Zaman, B.T.; Torkay, G.; Dönmez, M.; Kayın, İ.; Bakırdere, S.; Bal-Öztürk, A. Micro-wave-Assisted Hydrothermal Green Synthesis of Selenium Nanoparticles Incorporated with Hyaluronic Acid Methac-rylate/Gelatin Methacrylate Hydrogels for Wound Healing Applications. *Polym. Eng. Sci.* **2024**, *64*, 316–327. [CrossRef]
59. Ruan, Q.; Yuan, L.; Gao, S.; Ji, X.; Shao, W.; Ma, J.; Jiang, D. Development of ZnO/Selenium Nanoparticles Embedded Chi-tosan-Based Anti-Bacterial Wound Dressing for Potential Healing Ability and Nursing Care after Paediatric Fracture Surgery. *Int. Wound J.* **2023**, *20*, 1819–1831. [CrossRef]
60. Mirza, K.; Hasan, L.; Pracha, M.; Ahmad, T.; Sardar, M. Biocompatible and Ecofriendly Selenium Nanoparticles in Diabetes and Wound Healing. *Next Nanotechnol.* **2026**, *9*, 100366. [CrossRef]
61. Pei, Q.; Zhang, L.; Yang, Y.; Gao, C.; Ma, B.; Xi, Y.; Wang, L. Preparation and Bioactivities of Selenium Nanoparticles Based on a Polysaccharide from Dendrobium Huoshanense. *Front. Nutr.* **2025**, *12*, 1689214. [CrossRef]
62. Jones, D.; Park, D.; Anghelina, M.; Pécot, T.; Machiraju, R.; Xue, R.; Lannutti, J.J.; Thomas, J.; Cole, S.L.; Moldovan, L.; et al. Actin Grips: Circular Actin-Rich Cytoskeletal Structures That Mediate the Wrapping of Polymeric Microfibers by Endothelial Cells. *Biomaterials* **2015**, *52*, 395–406. [CrossRef]
63. Khalid, A.; Tran, P.A.; Norello, R.; Simpson, D.A.; O'Connor, A.J.; Tomljenovic-Hanic, S. Intrinsic Fluorescence of Selenium Nanoparticles for Cellular Imaging Applications. *Nanoscale* **2016**, *8*, 3376–3385. [CrossRef]
64. Steenbock, T.; Drescher, E.; Dittmann, T.; Bester, G. How Surface Defects Shape the Excitons and Photoluminescence of Ultrasmall CdSe Quantum Dots. *Chem. Mater.* **2024**, *36*, 6504–6514. [CrossRef]
65. Ferroudj, A.; Csík, A.; Prokisch, J. Allotrope-Dependent Physicochemical and Optical Properties of Red and Grey Selenium Nanoparticles. *RSC Adv.* **2026**, *16*, 20391–20398. [CrossRef]
66. Vinukonda, A.; Bolledla, N.; Jadi, R.K.; Chinthala, R.; Devadasu, V.R.S. Synthesis of Nanoparticles Using Advanced Techniques. *Next Nanotechnol.* **2025**, *8*, 100169. [CrossRef]
67. Redolfi-Bristol, D.; Yamamoto, K.; Zhu, W.; Mazda, O.; Riello, P.; Marin, E.; Pezzotti, G. Mapping Selenium Nanoparticles Distribution Inside Cells through Confocal Raman Microspectroscopy. *ACS Appl. Mater. Interfaces* **2025**, *17*, 18124–18133. [CrossRef]
68. Bissardon, C.; Proux, O.; Gazze, S.A.; Filhol, O.; Toubhans, B.; Sauzéat, L.; Bouchet, S.; Lewis, A.R.; Maffeis, T.; Hazemann, J.-L.; et al. Intracellular Fate of Sub-Toxic Concentration of Functionalized Selenium Nanoparticles in Aggressive Prostate Cancer Cells. *Nanomaterials* **2023**, *13*, 2999. [CrossRef]

69. Wang, H.; He, Y.; Liu, L.; Tao, W.; Wang, G.; Sun, W.; Pei, X.; Xiao, Z.; Jin, Y.; Wang, M. Prooxidation and Cytotoxicity of Selenium Nanoparticles at Nonlethal Level in Sprague-Dawley Rats and Buffalo Rat Liver Cells. *Oxid. Med. Cell. Longev.* **2020**, *2020*, 7680276. [CrossRef]
70. Qiao, L.; Yan, S.; Dou, X.; Song, X.; Chang, J.; Pi, S.; Zhang, X.; Xu, C. Biogenic Selenium Nanoparticles Alleviate Intestinal Epithelial Barrier Damage through Regulating Endoplasmic Reticulum Stress-Mediated Mitophagy. *Oxid. Med. Cell. Longev.* **2022**, *2022*, 3982613. [CrossRef]
71. Xu, C.; Qiao, L.; Ma, L.; Guo, Y.; Dou, X.; Yan, S.; Zhang, B.; Román, A. Biogenic Selenium Nanoparticles Synthesized by Lactobacillus Casei ATCC 393 Alleviate Intestinal Epithelial Barrier Dysfunction Caused by Oxidative Stress via Nrf2 Signaling-Mediated Mitochondrial Pathway. *Int. J. Nanomed.* **2019**, *14*, 4491–4502. [CrossRef]
72. Varlamova, E.G.; Goltyaev, M.V.; Maltseva, V.N.; Turovsky, E.A.; Sarimov, R.M.; Simakin, A.V.; Gudkov, S.V. Mechanisms of the Cytotoxic Effect of Selenium Nanoparticles in Different Human Cancer Cell Lines. *Int. J. Mol. Sci.* **2021**, *22*, 7798. [CrossRef]
73. Zhuang, Y.; Li, L.; Feng, L.; Wang, S.; Su, H.; Liu, H.; Liu, H.; Wu, Y. Mitochondrion-Targeted Selenium Nanoparticles Enhance Reactive Oxygen Species-Mediated Cell Death. *Nanoscale* **2020**, *12*, 1389–1396. [CrossRef]
74. Bartolomé, M.; Villaseñor, M.J.; Ríos, Á. Surface Plasmon Resonance Optical Sensors Involving Nanomaterials as Reliable Analytical Tools: A Critical View about Performance and Applications. *Anal. Chim. Acta.* **2026**, *1382*, 344693. [CrossRef]
75. Wallenberg, M.; Misra, S.; Björnstedt, M. Selenium Cytotoxicity in Cancer. *Basic Clin. Pharmacol. Toxicol.* **2014**, *114*, 377–386. [CrossRef]
76. Bao, P.; Chen, Z.; Tai, R.Z.; Shen, H.M.; Martin, F.L.; Zhu, Y.G. Selenite-Induced Toxicity in Cancer Cells Is Mediated by Metabolic Generation of Endogenous Selenium Nanoparticles. *J. Proteome Res.* **2015**, *14*, 1127–1136. [CrossRef]

Disclaimer/Publisher's Note: The statements, opinions and data contained in all publications are solely those of the individual author(s) and contributor(s) and not of MDPI and/or the editor(s). MDPI and/or the editor(s) disclaim responsibility for any injury to people or property resulting from any ideas, methods, instructions or products referred to in the content.